AZURA WEC power performance - a preliminary comparison of trial data and numerical modelling results

Krishnakumar Rajagopalan, Patrick Cross, Bradley Ling, and Terry Lettenmaier

***Abstract*—The U.S. Navy Wave Energy Test Site (WETS) in Hawai'i, the United States' first grid-connected test site of this kind, has been operational since 2015. The Hawai'i Natural Energy Institute (HNEI) at the University of Hawaii is providing key research support for this facility. This support includes advisory services to developers using numerical models and evaluating WEC designs. These services were leveraged in the case of the recent deployments of the Northwest Energy Innovations (NWEI) Azura WEC, the first device to be tested since the 2015 expansion of WETS to three test berths. Azura has now undergone two phases of testing at WETS, with key physical modifications to its hull and float between deployments to improve the performance. While NWEI conducted the modeling to achieve the design of these modifications, we specifically examine the impact they had on motion and power performance of the WEC – by comparing measured and modeled data. During the second phase of testing, which began in February/18 and continued until August/2019, it was observed that the device was not performing as expected in terms of power production. The focus of this paper is a preliminary analysis of the reasons for this suboptimal performance.**

***Keywords*—AQWA; AZURA; PTO; Response Amplitude Operator (RAO); Wave Energy Test Site; WEC-Sim.**

I. INTRODUCTION

WEC R&D is currently in a nascent stage. Although numerical modeling is an essential and useful tool in WEC design, experimental data are of primary importance for validating the model results and learning important lessons from physical experiments, at open ocean test sites such as WETS. Many developers are reluctant to publish power production data; however, over the past several years, some WEC developers have either published power data and other relevant information online [1], or power performance results are available in journal and conference publications [2][3]. These resources offer WEC developers a treasure trove of data to design, test and develop their WECs. At HNEI, which has a mandate for renewable energy technology development, the Azura prototype testing gave an opportunity for understanding the evolution of a WEC from its numerical design stage to actual ocean testing. In this paper we share some of the lessons learned from this ocean testing, which took place at WETS.

The baseline Azura device – which consists of a float and a spar – was deployed at WETS during 2015-2016 at the 30m berth [4][5]. The spar provides a reaction point against which the float rotates. A Power Take Off (PTO) located at the hinge generates power from the relative rotation of the spar and float. The mass of the spar is roughly ten times that of the float. A modified version of the device -which consists of a modified float, and spar augmented with a heave plate- was deployed in 2018, also at the 30m berth. See Fig. 1. The modifications were expected to improve the performance of the device. The baseline device and modified prototype are considered half scale by the NWEI design team who are leveraging test data collected from the deployment to improve the performance of the device while developing the full scale prototype.

Numerical modeling of power performance carried out both at NWEI and HNEI independently, prior to deployment, predicted a factor of two to three improvement from the baseline device to the modified prototype. A motivation for this paper is to understand why this expected improvement was not realized during deployment of the modified prototype. In this paper we include some preliminary findings that could explain this discrepancy. Let P_b denote the electric power generated by the baseline device in regular waves of height 1m and period of ≈ 6s, in watts; then maximum electric power generated by this (baseline) device was about $1.6P_b$, in irregular seas during the deployment period in year 2016. (In this study we only report 30 minute average power). In the case of the modified prototype, in spite of the modifications, electric power did not exceed P_b, during deployment last year. This paper is a preliminary step in

ID 1530 track WHM

Dr. Krishnakumar Rajagopalan is an Assistant Researcher at the Hawaii Natural Energy Institute, University of Hawaii, 1680 East-West Rd, Honolulu, HI 96822. (e-mail: krishnak@hawaii.edu)

Dr. Patrick Cross is a Specialist at the Hawaii Natural Energy Institute, University of Hawaii, 1680 East-West Rd, Honolulu, HI 96822. Dr. Cross is also the Program Manager for University support to the Wave Energy Test Site (WETS).

Mr. Bradley Ling is the R&D Engineer at Northwest Energy Innovations (NWEI), 1211 NW Glisan Street, Oregon, 97209

Dr. Terry Lettenmaier is the Consulting Engineer (for NWEI) and founder of Williwaw Engineering, South Beach, Oregon, 97366

explaining the discrepancy in performance of the modified prototype. We examine the device hydrodynamics, as set by the geometry, and the PTO operating regime as probable causes for suboptimal performance of the modified prototype.

Briefly, the PTO unit of the Azura device consists of a generator and a hydraulic system, which drives this generator. This PTO can be in the 'on' or 'off' state. In the 'on' state, the hydraulic system, the displacement motor and the generator, all work in tandem generating electric power. When the PTO is 'off', there is no power generation. However, the hydraulics are still active, resulting in some power loss. Additionally some losses also occur in the bearings at the hinge in both the on and off states. The PTO is instrumented in such a way that the hydraulic losses can be estimated from deployment data but there is no way to measure bearing losses.

In this paper, we focus on the experimental data obtained from the modified prototype device (Fig. 1(b)) when it was deployed at WETS during 2018 (February to August). The experimental data consist of the spar motions, which are heave, pitch, roll and heading, the float pitch and electric power data. Response Amplitude Operators (RAOs) are estimated from the experimental data for those motions that primarily contribute to power generation. On the basis of the experimental RAOs, and the actual electric power delivered by the modified prototype during last year's deployment, we present a *preliminary* hypothesis on why the device did not perform as expected.

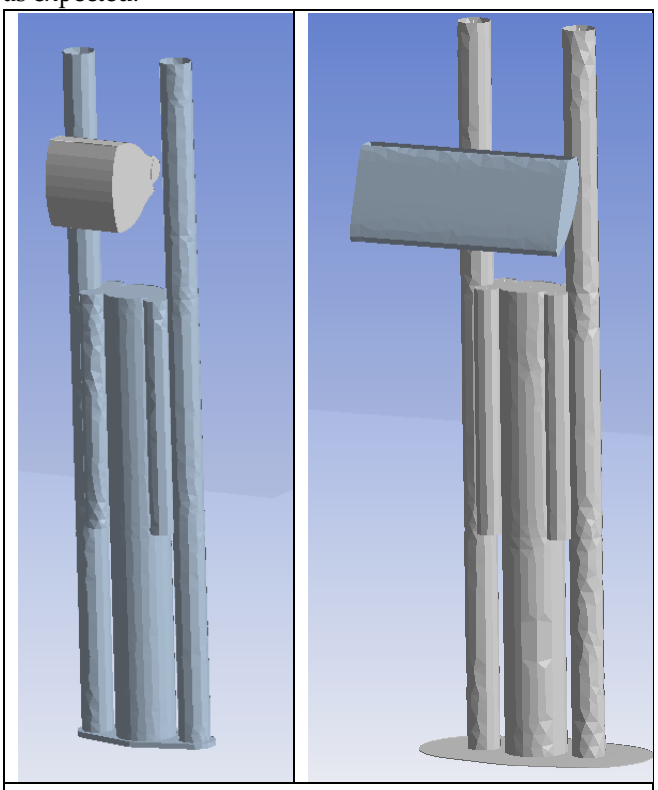

Figure 1: Baseline device (Left). Modified prototype (Right). Modifications consist of addition of a heave plate to the spar and replacement of the original float with a new one that has an entirely new geometry

First, the experimental RAOs when the PTO is off are estimated. Then numerical modeling is carried out using Boundary Element Method (BEM) software, e.g. NEMOH, In-house code, WEC-Sim and ANSYS AQWA, and comparisons are made between the experimental and numerically computed RAOs. Agreement between numerical results and experimental data, when the PTO is off, would form a basis for later inclusion of a linear PTO or losses in the hydraulic system. RAOs of the device when the PTO is 'on' are also computed.

Next, the numerical model of the hydraulic, non-linear PTO, which is compatible only with MATLAB—which was developed by NWEI and provided to HNEI—is linearized using WEC-Sim. This is required as the AQWA software can only model a simple linear (rotational) PTO. In this study most of the regular wave simulations are set up in WEC-Sim. AQWA is used for the irregular wave runs. We found that AQWA is significantly faster than WEC-Sim for irregular wave simulations and can also easily incorporate the full mooring of the device.

Based on the difference in RAO between the two states –PTO on and off- and the corresponding difference in electric power seen in experimental data as well numerical results, probable causes for the suboptimal performance of the modified prototype is given.

II. Experimental Results

During the deployment at WETS, the device had its PTO in the 'on' state during most of the period. There were also a few days when the PTO was fully switched off. Experimental data for device motions during this period are studied, to obtain the RAOs of the device alone—without much loss in the PTO. The outcome—experimental RAOs without much loss in the PTO—can be a *fundamental check* for all numerical models [6]. Below, we focus on the following days, April/14/2018 (over 11 hours of data) and March/22/2018 (over 16 hours of data) when the PTO was in the off state.

(a) PTO 'off'

The RAO is calculated from the point wave amplitude spectrum, S_η, and the response spectrum of the device motion. Let η_3 and η_5 denote the heave and pitch respectively of the spar, and η_{11} denote the pitch of the float. These motions have conventional directions, as in Lewis [7]. For example, the spar heave $RAO_{\eta 3}$ is then [7]

$$RAO_{\eta 3} = \sqrt{\frac{S_{\eta 3}}{S_\eta}} \qquad \text{Eq. 1}$$

In Eq. 1, $S_{\eta 3}$ is the heave response spectrum of the device. Similarly for other motions, η_5 and η_{11}. The WETS Waverider CDIP buoy is used to obtain point wave spectra [8]. Each CDIP wave spectrum is calculated with 30 minutes of wave elevation data measured by the buoy. As the 30m berth site is about a mile south east from the location of the Waverider buoy, which is at 80m, the incident wave spectra has been corrected for shoaling, using linear wave theory, for the difference in depth

between the buoy and Azura locations. In addition to the spectra, the wave rider data also include peak wave direction.

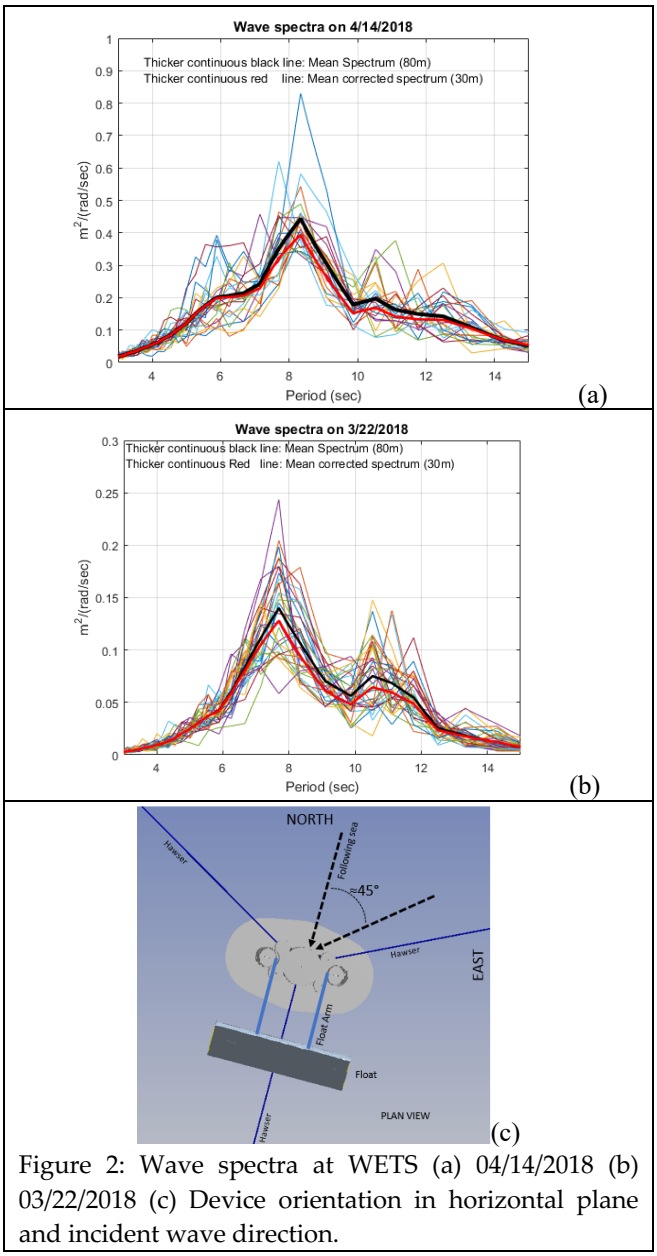

Figure 2: Wave spectra at WETS (a) 04/14/2018 (b) 03/22/2018 (c) Device orientation in horizontal plane and incident wave direction.

Figs. 2 (a) and (b) show wave spectra from April/14/2018 and March/22/2018, respectively. Fig 2 (a) has 22 wave spectra and Fig 2(b) has 32 wave spectra. Shown in Fig. 2 (c) is the orientation of the device in the horizontal plane and the incident wave direction. The float is downstream of the Spar. Following seas would correspond to about 20º from North in Fig 2(c).

The significant wave height, H_s, and peak period, T_p, of the mean corrected spectrum are 1.93m and 8.3s respectively for 04/14. The corresponding values for 03/22 are 1.0m and 7.7s. The higher sea state in Fig. 2(a) can be attributed to the Trade Winds since energy peak occurs near 8s. These winds are prevalent at the WETS test site. During the winter season in the northern hemisphere, the site also experiences large wave events from northern swells. The sea state shown in Fig 2(b) is comparatively mild, but is also predominantly forced by the Trade Winds. The peak wave direction in Fig 2(a) ranges from 11º to 72º, with a mean of 60º. The corresponding values in Fig 2(b) are 24º to 78º with a mean also of 60º. From the mean peak wave direction data, the incident waves are from mostly ENE, whereas the device is aligned roughly NNE. The absolute response (not the RAO) of the device on these two days can be expected to be different due to the large difference in the incident wave energy. The area under the mean spectrum from a wave period range of 3 to 15 seconds, contributes 96% of the energy density in Fig 2(a) and over 99% in Fig 2 (b). Additionally the PTO mechanism is not efficient outside of this period range. This justifies focusing on the wave period range of 3s to 15s, to study various aspects of the device.

The WAFO toolbox [9], which can be paired with MATLAB or GNU OCTAVE, is used to calculate the device response spectrum. The *dat2spec* function of this toolbox, with a Parzen window of lag size L_{max}, was applied to estimate the device response spectrum. L_{max} determines the smoothing of the spectrum. Following the guidelines in the WAFO tutorial for determining L_{max} based on the covariance function, a value of 1000 was chosen as the best smoothing parameter. Using a smaller value, say 500, makes the spectrum appear smoother but also results in loss of some trends. From the device response spectra, the various RAOs are calculated using Eq.1. Figure 3 shows the spar heave RAO calculated on the two days, which are, April/14 (black shade) and March/22 (grey shade). As can be seen from Eq. 1, the direction of the waves is not explicitly taken into consideration while calculating the RAOs. However, the predominant direction of the waves is reproduced in the AQWA numerical model (explained later in Section III). Also, the method of calculating the numerical and experimental RAOs are similar. This leads us to believe that no special treatment is required while dealing with wave direction.

The spar heave RAO is small, less than 0.5, below 10s, but increases rapidly to around 2 as the wave period approaches 15s. There is good agreement between data from the different days, especially at smaller periods, although the incident wave energy is much larger on 04/14. Ideally, the RAO from all wave spectra would lie on an identical curve. We see from Fig. 3 that there is noticeable scatter in RAO results at longer periods. Also, this scatter is larger for data from 03/22, when the incident wave energy is smaller. Noting that in Eq. 1, the incident wave energy appears in the form of the spectral density in the denominator, a possible cause for the scatter of the RAOs could be the lesser energy for the wave spectra at longer periods [10]. Reinforcing this argument is the increased scatter in RAO results from 03/22, when incident wave energy is smaller. Similar scatter is also seen in the spar and float pitch results. Yet another cause for scatter is the stochastic nature of the experimental data itself. We can then infer that there is some uncertainty in RAO results at longer periods. However, this fact is not expected to affect the results in this paper, as the power production from the

PTO is insignificant at the longer periods where scatter in RAO occurs.

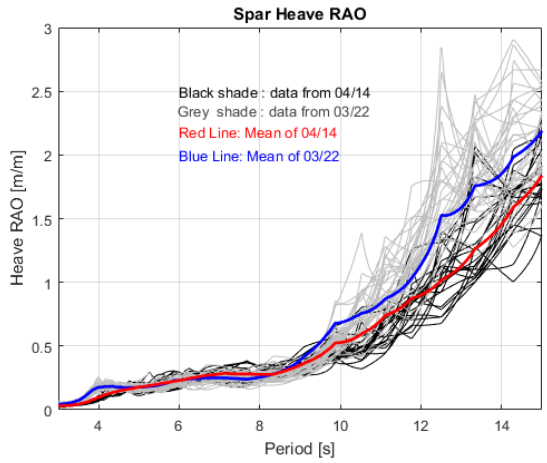

Figure 3: Spar Heave RAO (Modified prototype). Black and grey shades represents data from 04/14 and 03/22 respectively.

Fig. 4 shows the Float RAO for both days. Also plotted in the figure is the mean RAO obtained by averaging the individual RAOs. It is pointed out that the float pitch angle, η_{11}, also equals the rotations of the float arm that connects the float to the spar (see Fig. 2c). The relative rotation between the spar and float (or float arm) drives the PTO unit. We observe a clear trend in the float RAO: there is resonance at ≈ 4sec. At this point the mean rotation of the arm is ≈ 20-25deg/m. The float rotations then decrease and reach a minimum value at a wave period of around 8sec, gradually increasing thereafter for longer wave periods. Comparing Figs. 2 & 4, it is clear that the float resonance does not occur in the wave period region where most of the incident wave energy is present. The spar pitch RAO is also shown in Fig. 4. This RAO is small and approximately 2.5deg/m in the wave period range shown.

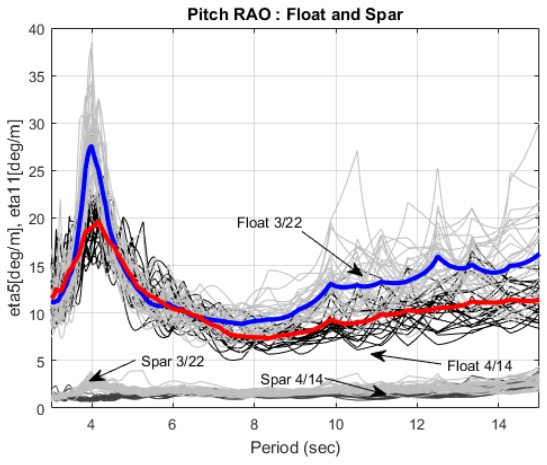

Figure 4: Black shade, RAOs (04/14); Grey shade, RAOs (03/22); Red line: Mean Float RAO (04/14); Blue line: Mean Float RAO (03/22). Spar Pitch RAOs are also plotted in lower part of figure.

(b) PTO 'on'

We focus on experimental data during the evening of April/14 and most of April/15 when the PTO was in the on state. By choosing these days, we look at the two states of the device, when the PTO is on or off, in similar wave conditions. The PTO 'on' analysis is based on 27 wave spectra. Without repeating details about calculations, which are in the previous sub section, we compare the mean RAOs in Figs. 5 (a) to (c). From these figures, we see that the heave RAO is marginally higher with the PTO on, when period is between 7 & 13s. The spar pitch remains small in both states. There is noticeable difference in the float pitch (and consequently the relative pitch) RAOs in the two states. For most of the period range, the RAO in the 'on' state is smaller. See Fig. 5(c). This is the expected result as electric power generation is a form of damping, resulting in smaller (rotational) motion for the float. However the differences are proportional to the magnitude of power generated. While quantifying the differences in RAOs we need to consider the electric power output of the device, which was about ≈ $0.4P_b$, during this period. In the following sections we check, using the numerical model, if we can quantify the *difference* between the RAOs in the two states (on and off) and relate that to electric power generated.

III. NUMERICAL MODELS

To understand the experimental results, we begin by studying the motion response of the device (RAOs) calculated from numerical models in regular and irregular waves. RAOs are calculated from (a) In-house model that uses linear hydrodynamics—calculated with BEM—and constraint equations to model motion response of the two body device in the time domain, without including viscosity [11], (b) WEC-Sim model [12], which uses linear hydrodynamics calculated with BEM, and Froude-Krylov (FK) and Hydrostatic loads based on instantaneous wetted surface area, while also including viscosity—modelled as drag force term in Morison's equation, thus nonlinear—, and (c) ANSYS AQWA, which is similar to WEC-Sim for the calculation of forces. In AQWA, the complete mooring of the device is also included. For (a) & (b), only regular wave forcing in following seas is considered. The wave steepness, defined as the ratio of wave height to wave length, is ≈ 0.01. However, in AQWA, irregular seas with actual spectra at WETS and peak wave direction are also included.

An important input for (b) & (c) is the viscous drag coefficient, C_d, of the spar and float, which affects the energy dissipation and thus the motion of these bodies, especially at resonance. The spar can be considered to be made of a group of cylinders with a plate connected to the end, for purposes of assigning a drag coefficient. In many cases C_d data are published as a function of the Keulegan Carpenter number, KC, which is defined as $KC = 2\pi\frac{A}{D}$, where A can be the amplitude of the incident wave (or the amplitude of the device motion in a quiescent fluid) and D

can be a reference diameter. We have approximated *KC* to get an estimate of the drag coefficient.

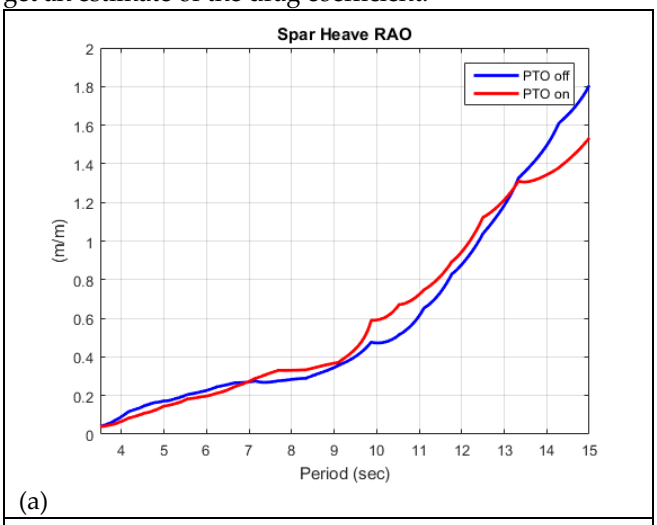

(a)

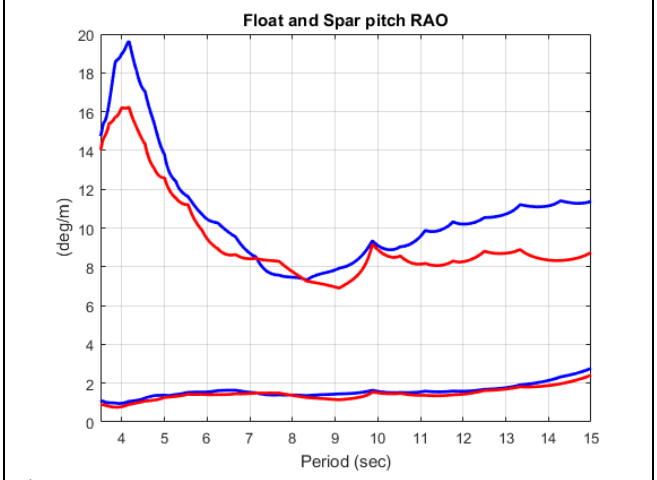

(b)

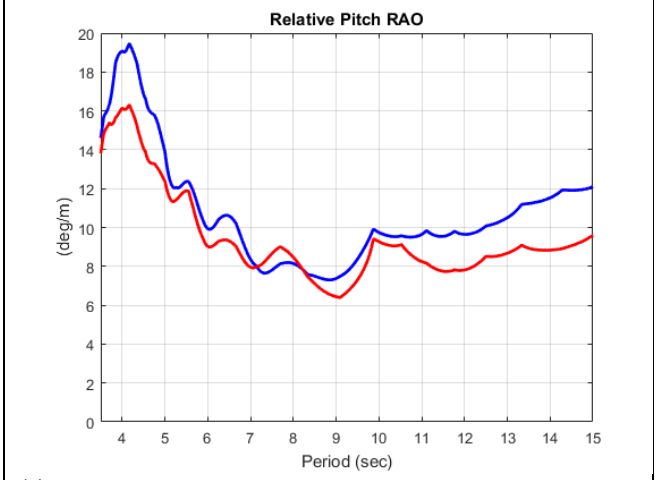

(c)

Figure 5: Comparison of experimental RAOs in the PTO on and off states. Blue and red lines represent the PTO off and on states respectively. Experimental results only.

The *KC* number is about 1 in our case. Tao and Dray [13] and Rajagopalan and Nihous [14] carried out experimental and numerical experiments respectively on circular plates. From these publications, at *KC* ≈1, the drag coefficient of the plate is about 5. In the parametric studies for drag presented later in this paper, this value ($C_d \approx 5$), is included. In a similar manner, the C_d of cylinders (that make up the spar) is taken to be about 1. It is pointed out that drag of a cylinder has a smaller variation than that of a plate, see Figs. 11 & 13 of Keulegan & Carpenter [15]. Thus, it is less onerous to carry out a parametric study involving cylinder drag coefficient. The values of C_d given above are only used as a guide in the parametric study as it is not straightforward to assign drag coefficient in an irregular sea where the incident wave amplitude varies greatly.

Choosing a drag coefficient for the float is considerably more difficult than the spar since published results for drag coefficient are not available for this geometry. The float has a large frontal area and small thickness (See Fig. 1), allowing it to be approximated as a thin plate. However due to the large uncertainty in its drag coefficient, we have carried out a thorough parametric study on its C_d.

Extensive parametric studies of float and heave plate drag were carried out with WEC-Sim. Numerical results, when wave period is away from resonance, were also checked with the In-house code. WEC-Sim simulations indicated that higher drag for the float and spar heave plate resulted in better agreement with experimental results. Note that for comparing with WEC-Sim results, we used experimental data in PTO 'off' state, while no rotational damping was included in the numerical models. Details are given in [6].

ANSYS AQWA model: When connected to the mooring [16], the external loads on the device consist of first order wave load, F^1, second order wave drift load, F^2, current load, F_C, wind load, F_W, and mooring cable load, F_m [17]. F^1 is the sum of Froude-Krylov and diffraction forces. F_C and F_W are modeled as drag force term in Morison's equation. The complete mooring is modelled. Fig. 2(c) shows the plan view of the device connected to the mooring. Risers connect fixed anchors to positively buoyant sub-surface floats, which are positioned about 10m below the still water line. Hawsers then connect the floats to the spar of the device. The mooring cable which consist of the ropes - Risers and Hawsers- and the subsurface buoy is modeled as a dynamic composite catenary line [17] that exerts a force, F_m, on the device. The forces on the rope consist of gravitational force, buoyancy force, structural inertia force, radiation force due to added mass, drag force due to current or cable motion, linear or nonlinear axial tension, and reaction at anchor and structural ends. The forces on the buoy are buoyancy/gravity force, structural inertia force, drag force due to current/buoy motion and radiation force due to added mass. The equation of motion of the Azura device in the time domain is [17],

$$\{\boldsymbol{M}+\boldsymbol{A}_\infty\}\ddot{\boldsymbol{X}}(t)=\boldsymbol{F^1}(t)+\boldsymbol{F^2}(t)+\boldsymbol{F_c}(t)+\boldsymbol{F_w}(t)+\boldsymbol{F_m}(t)-\boldsymbol{KX}(t)-\int_0^t \boldsymbol{h}(t-\tau)\ddot{\boldsymbol{X}}(\tau)d\tau \qquad \text{Eq. 2}$$

In Eq. 2, t represents time, $\boldsymbol{M}$ is structural mass matrix, $\boldsymbol{A}_\infty$ is the added mass matrix at infinite frequency, $\boldsymbol{X}$ and its (time) derivative represent displacement and acceleration. $\boldsymbol{K}$ is the hydrostatic stiffness matrix. The $\boldsymbol{A}_\infty$ term and the

last term in Eq. 2 arise from using the convolution integral for calculating the radiation forces [17]. The rest of the terms were described previously. $\boldsymbol{F^1}$, $\boldsymbol{F^2}$, radiation forces, and $\boldsymbol{K}$ are calculated in Aqwa using a Boundary Element Method.

Based on the parametric study for drag coefficient carried out with WEC-Sim, we examine three scenarios. In one, the drag of the spar heave plate and float are both small, $C_d \approx 1.15$, and equal the AQWA-recommended value; in the second, drag coefficients are high, ≈ 5; and in the last, C_d of the float is high whereas C_d of the heave plate is small. Table 1 shows the case studies carried out with AQWA.

TABLE 1: Case Study for AQWA runs, wave incident angle ≈ 45º

DRAG COEFFICIENT FOR FLOAT AND SPAR HEAVE PLATE
Low drag for float and heave plate
High drag for float and heave plate
High drag for float and low drag for heave plate

Since the Waverider spectrum is calculated from 30 minutes of wave surface elevation data, the AQWA runs are also for 30 minute duration. Using the surface elevation from the numerical model and the WAFO toolbox, we calculate the spectra actually generated within the numerical model. Based on the device motions for spar heave and pitch, and float pitch, the response spectra are estimated. Using Eq. 1, the RAOs are then calculated. In all cases the incident wave is about 45º east of the device orientation. See Fig. 2(c). Fig. 6 (a) shows the achieved spectra from the model, and the target spectra. It was found that there is some ringing observed in the achieved spectra (from the AQWA model) at short periods, < 3.5 to 4s. Using a shorter lag for the Parzen window smooths out this ringing, but it also results in loss in some trends in the spectra. Since the focus is on calculating the transfer function (RAOs), an exact replica of the target spectra is not required to be generated. For AQWA runs, we have carried out a limited study on phase angle and duration of physical simulation time (30 minutes or 3 hours). The phase angle determines the phase of spectral components in AQWA.

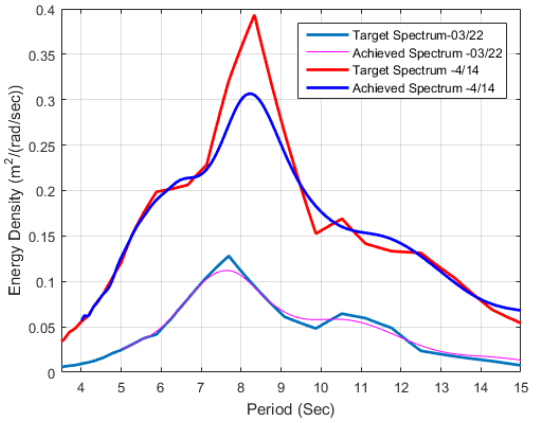

(a)

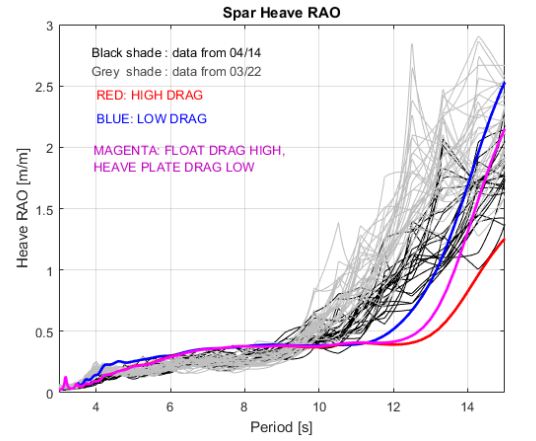

(b)

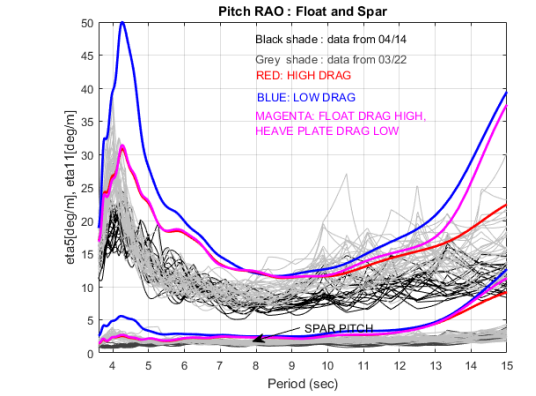

(c)

Figure 6: (a) Comparison of achieved spectrum in AQWA model and (mean) target spectrum on 03/22 and 04/14. (b) Comparison of numerical and experimental heave RAO. (c) Comparison of numerical and experimental pitch RAO

Comparison of spar heave experimental and numerical RAOs is given in Fig. 6(b). For AQWA model, only results from 04/14 are included, mostly for clarity in the figures. We see that irrespective of the drag coefficient, there is good agreement between experimental and numerical heave RAOs until around 10s. Beyond this period, the smaller drag configuration follows the experimental trend. The float pitch and spar pitch RAOs are given in Fig. 6(c). It clearly shows that the larger drag for the float drastically reduces its motion, especially at resonance around 4s. Generally the larger drag case agrees better with

experimental data throughout the period range. There is good agreement with experimental data when period > 7s for the larger drag case. For shorter periods, the agreement is reasonable, although it could be better. For the case where the drag of the float is high and that of the heave plate is low, deviation of numerical float pitch RAO from experimental RAO at longer periods is not small. This case also agrees closely with the larger drag case at shorter periods and with the lower drag case at longer periods. In the case of spar pitch RAO, there is good agreement between the experimental data and numerical results until around 12s. Beyond that numerical results diverge from the experimental data.

IV. Linearization of Hydraulic PTO

The numerical model of the hydraulic PTO was developed at NWEI and provided to HNEI. This model has some similarities to that published by So, et. al [18] but the NWEI PTO configuration is different. The NWEI PTO model, developed by Mr. Bradley Ling of NWEI, was developed to accurately model the dynamics of the NWEI hydraulic PTO. Performance of the PTO model was validated by comparing it to experimental data [5]. This model is compatible with MATLAB/WEC-Sim (and not with AQWA).

The actual PTO (not the model) outputs several variables including the electric power, P_{e_n}, and the power consumed in the hydraulics, P_{h_n}, can be calculated from flow rate and pressure. (Here the subscript $_n$ stands for non-linear). The efficiency of the PTO, η_{pto}, is well documented in the trials, meaning, $P_{e\_n} \approx \eta_{pto} P_{h\_n}$.

The need to linearize the NWEI PTO model arises from the fact that the AQWA software can only account for a linear PTO. Given a rotational damping coefficient, (with units, $\frac{Nm}{c/s}$), this linearized PTO provides a torque (product of damping coefficient and relative rotational velocity) and consumes mechanical power (product of damping coefficient and square of relative rotational velocity). Thus a (linear) rotational damping coefficient emulates the hydraulic PTO. To calculate the electric power from the mechanical power generated by the linear PTO, the PTO efficiency, η_{pto}, is used. Thus, $P_{e\_lin} \approx \eta_{pto} P_{m\_lin}$, where, P_{e_lin} is the electric power and P_{m_lin} the mechanical power of the linear PTO.

The first step in linearization is to obtain the Quadratic Transfer Function (QTF) of electric power from the NWEI PTO model in regular seas, using WEC-Sim. Then the numerical runs are repeated with a *linear* PTO, until a certain damping coefficient generates an electric power QTF close to that of the NWEI PTO model. The linear PTO is also set up in WEC-Sim (but AQWA could also be used).

For calculating QTF in regular waves, inputs include wave height and period. For the wave energy prize [19], wave steepness -defined as H/L, where H denotes the wave height and L denotes the wave length- of 1/25 (0.04) and 1/40 (0.025) were chosen in regular (monochromatic) waves. Knowing the steepness and wave period, the (wave) height can be calculated. In this study we use a different approach to set the wave steepness for regular waves. It is pointed out that the magnitude of the QTF itself can change for a non-linear PTO as the wave height is varied, for a given period. Thus it is important to know realistic wave height as a function of period. Also, considering that we can get an approximate idea of the power in irregular seas by simply multiplying the wave amplitude spectrum and QTF (followed by a few simple operations), a 'better' estimated QTF can be very useful.

First we examine wave steepness in real seas. This information is then used to set wave height in numerical models when running regular waves. Fig. 7 shows the average wave steepness [9], S_s, as a function of energy period, T_e, calculated from WETS Waverider buoy data. From this figure, we see that at shorter energy periods, the average steepness is larger with an average value of about 0.04, and at longer periods, this reduces to about 0.01. Although we cannot make a direct comparison between spectral sea and regular waves, we can use Fig. 7 as guidance for setting wave height (or steepness) of regular waves. Thus for regular wave simulations in this study, wave heights were based on the mean S_s curve shown as the continuous black line in Fig. 7.

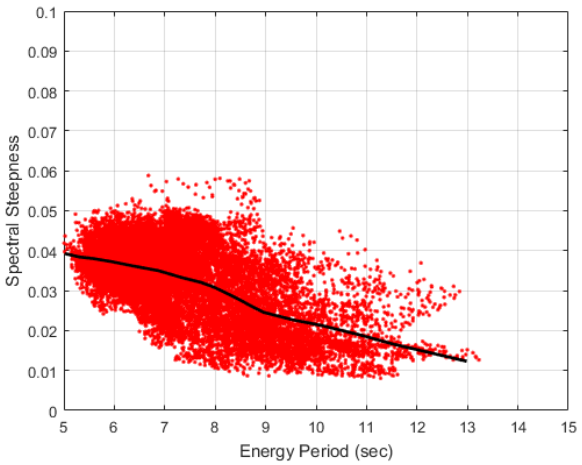

Figure 7: Average wave steepness as a function of energy period. The continuous black line represents average of the red data points at any period. Data from WETS wave rider buoy.

For regular wave runs in WEC-Sim with PTO (linear and hydraulic), to calculate QTF, we have chosen the case where the drag coefficient of the float as well as the spar heave plate is high, as this case gave best agreement with trial data. Fig. 8 compares QTF divided by P_b, (see Introduction for definition of P_b) for the hydraulic NWEI PTO, and the linear PTO models. Let C_b denote the rotational damping coefficient, with units of $\frac{Nm}{c/s}$, that was previously utilized to predict electric power for the *baseline* device in irregular waves at HNEI. We report the value of the damping coefficient as a fraction of this C_b in this study. Values of damping coefficient vary from 0.16 C_b to 1.33 C_b in Fig. 8. Also included in Fig. 8 is the wave amplitude spectrum from Section II, with H_s of 1.93 and T_e of 8.3s. An

ideal case is when the peaks of spectrum and QTF coincide. Also larger values of QTF occur where wave energy is comparatively smaller.

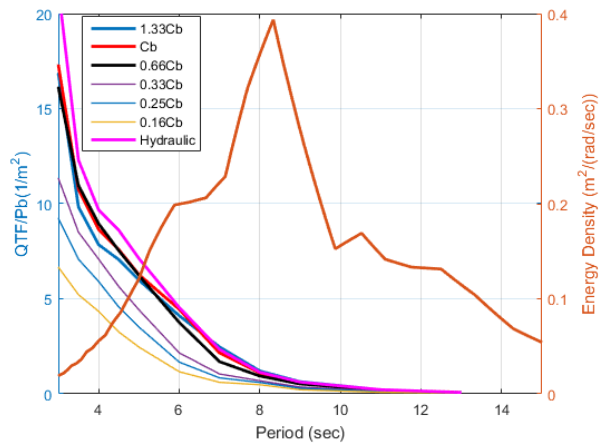

Figure 8: Left y- axis points to QTF/P_b. Right y-axis points to wave amplitude spectrum.

We now calculate electric power in irregular seas from the linear PTO, for different values of damping coefficients, and the hydraulic PTO, to choose the best damping coefficient. This is done by multiplying the QTF by the wave amplitude spectrum, followed by a few operations (See Eq. 9 of [20]). See Table 2.

Table 2: Electric power estimated from QTF and spectrum

Type of PTO	Rotational Damping Coefficient	Electric Power divided by P_b
Linear PTO	$0.16C_b$	≈0.60
"	$0.25C_b$	≈0.90
"	$0.33C_b$	≈1.10
"	$0.67C_b$	≈1.60
"	C_b	≈1.65
"	$1.33C_b$	≈1.60
Hydraulic PTO	-	≈1.86

From Table 2, when damping coefficient is C_b, difference in electric power output between the linear and hydraulic PTO is the smallest, so this value is chosen as the optimum damping coefficient. By comparing power obtained with damping coefficient, C_b, which equals 1.65 P_b in Table 2, and, during trials, we get an indication of the degree to which the performance might have been better.

V. Numerical Model Update for PTO 'off' Condition

In section II, the numerical model when PTO is 'off' was established. It was also pointed out that the power consumed in the hydraulics of the actual device in this condition was not included in the numerical model. A review of experimental data in this condition reveals that the power consumed in the hydraulics is about $0.08P_b$ to $0.16P_b$. Including frictional losses at the hinge, we take the total power lost to be about $0.2P_b$. Accordingly the numerical model was updated to include a linear damping such that the power dissipated agrees with experimental data. Fig. 8 and Table 2 were used as a guideline to set the damping coefficient. Fig. 9 below shows the updated result. As the power consumed was only ≈ $0.2P_b$, the updated results are not very different from earlier ones. We also note that there is some difference between the numerical results and experimental data in this (PTO 'off') condition, at the shorter periods, even after the power loss in the hydraulics is included in the numerical model. From here onwards, we focus on relative pitch RAO for explaining suboptimal performance of the modified prototype, noting that relative pitch is the difference between the float and spar pitch motion.

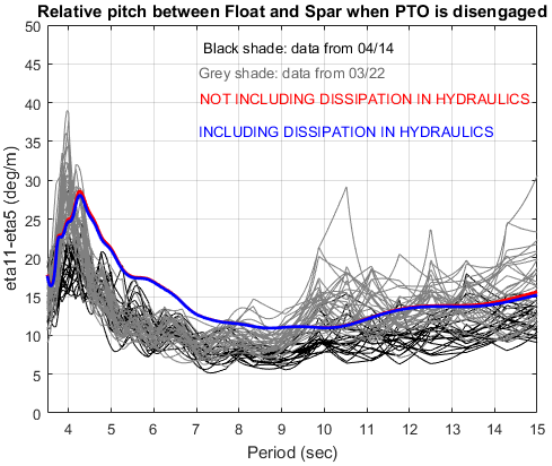

Figure 9: Relative pitch RAO when the device is in the 'off' condition.

VI. Comparison of Electric Power –Data and Numerical Results

We ran the AQWA model that included a linear PTO with different damping coefficients, in irregular waves. These irregular waves had spectral characteristics similar to actual seas encountered during the period when the experimental data was taken. Fig. 10 (a) shows results for relative pitch as the PTO damping is varied. Also included in this figure is the result when the PTO is 'off' -this corresponds to $0.02C_b$. Further the electric power developed by the device for different damping coefficients is given in Fig. 10(b). With the optimized PTO, when damping equals C_b, the electric power would be $1.25P_b$ (for the modified prototype). Under similar conditions the baseline device generated about $0.8P_b$. We now argue that the *difference* in relative pitch RAO in the PTO *on* and *off* states, can give us an indication of the electric power generated. This difference is plotted in Fig. 10(c) for various (PTO) damping coefficients. Also included in Fig 10 (c) is the difference calculated from *trial* data, when the device was generating about $0.4P_b$, electric power.

From Fig. 10 (c), we infer that the effective damping of the modified prototype PTO in trials (black curve in Fig 10(c)), was significantly smaller than modelled. In fact, trial results are closer to the AQWA model with damping ≈ $0.16C_b$. With this damping coefficient the electric power from trials and model also agrees.

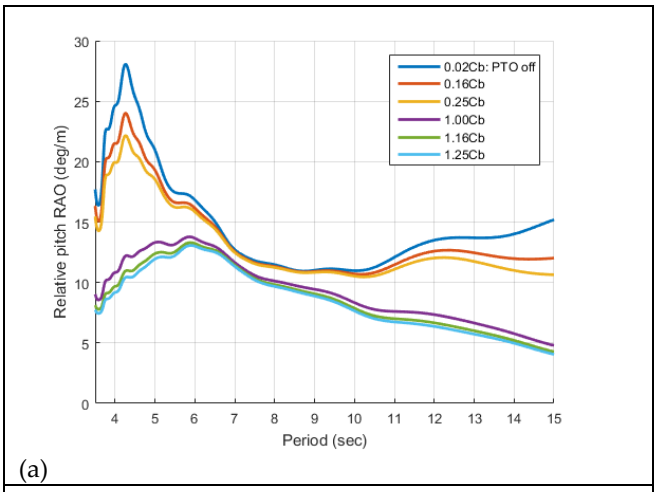

(a)

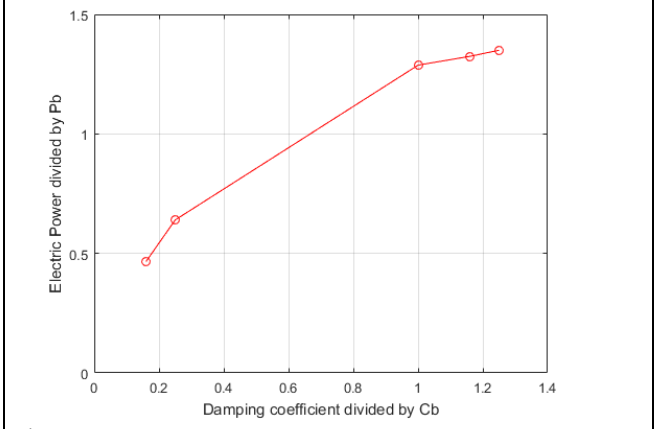

(b)

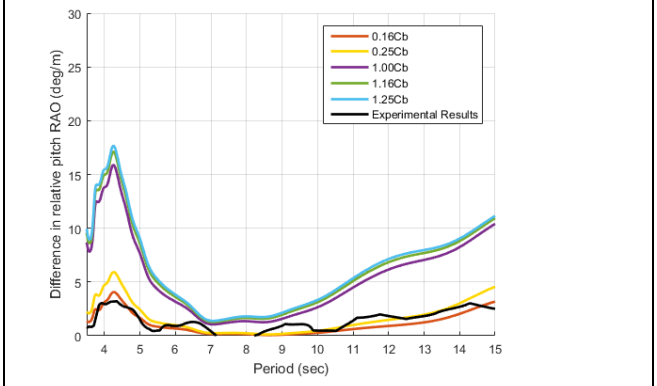

(c)

Figure 10: (a) AQWA irregular wave results for relative pitch RAO for various damping coefficients. (b) Electric power vs damping coefficients for cases in (a). (c) Difference in relative RAO. Numerical results and experimental data. In both cases, differences are from the PTO 'off' condition.

It has already been shown that there is reasonable agreement between the numerical model and actual device hydrodynamics (See Fig. 9) in the PTO 'off' condition. Additional changes in motion RAOs are produced by the PTO damping. So it is highly likely that it was the actual PTO hardware that was incapable of producing the required damping. Noting that for both the baseline device and modified prototype the same PTO was used, let us examine the loadings on the PTOs in the two cases—baseline device and modified prototype—for insight into probable causes of its insufficient damping (when fitted to modified prototype). For this purpose we include the QTF of the Baseline device in Fig. 11(a). Once again, from this figure, calculating electric power in waves using wave amplitude spectrum and QTF, the output of modified prototype device is $1.65P_b$ whereas that of baseline device is about $0.7P_b$. Fig. 11(b) shows the cumulative power for modified prototype and baseline device as a function of wave period. For example, 55% of $1.65P_b$ (modified prototype) comes from periods shorter than 5s, whereas this number is only 25% for the baseline device. Thus, we note that the PTO when fitted to the modified prototype was required to outperform at shorter periods – a clear difference with the baseline device.

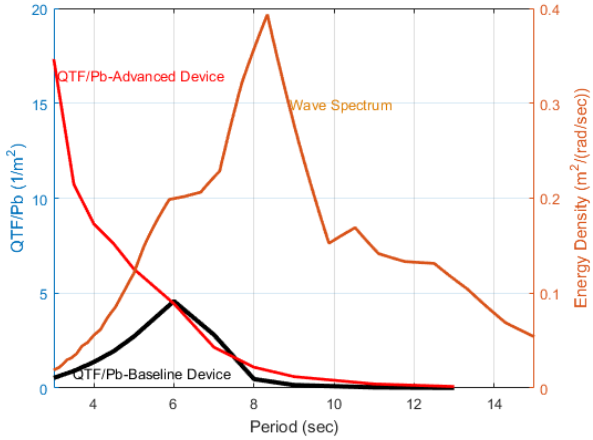

(a)

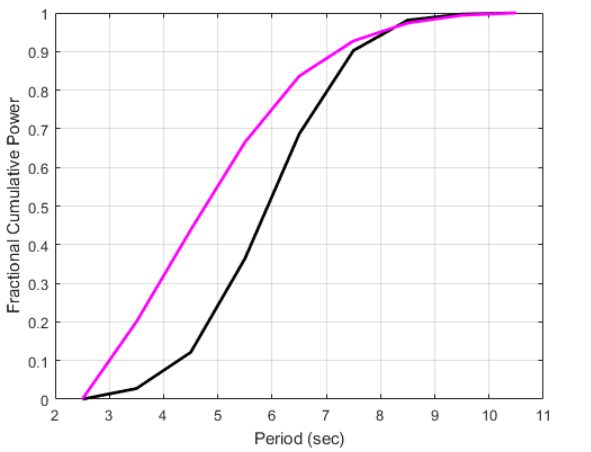

(b)

Figure 11: (a) QTFs of Modified prototype and Baseline device. Also shown in (a) is the wave amplitude spectrum. (c) Fractional cumulative power: Magenta -> Modified prototype, Black-> Baseline device.

Since both QTFs in Fig. 11(a) were generated with linear PTO with damping of C_b, and since torque is a product of C_b and relative angular velocity, we also note that the torque required to be generated in the modified prototype was much larger and it (the torque) was required to be generated at shorter periods. Thus, the operating regime of the PTO shifted towards shorter periods in the modified prototype. In reality, the QTF of the modified prototype during deployment resembled the curve represented by 0.16Cb in Fig. 10 (a), indicating that the actual performance

of the PTO may have been below expected levels throughout the period range of interest.

Examination of NWEI PTO trial data indicated that there was no failure of the PTO between deployments. The implication is that the PTO was simply not capable of performing as modelled in this rapid cycling high torque environment. It is also noted that the bearing friction in the modified prototype may have been larger, primarily due to the change of shape of the float. This may also have contributed to some loss of performance. We have used a linear PTO for drawing many of the conclusions. There is a level of approximation when the PTO is linearized, however this approximation is not expected to change the larger conclusions.

VII. Conclusion

The study examines probable causes for suboptimal performance of the modified prototype AZURA device during its deployment at WETS. Numerical runs are set up in AQWA that include drag parametric studies to model the device in PTO 'off' condition. The numerical model is also set up in WEC-Sim for linearization of the NWEI PTO model, so that the AQWA model can emulate the hydraulic PTO. The difference in relative pitch RAO in the PTO 'on' and 'off' conditions is calculated in the trial data. This difference is then reproduced in AQWA runs. The study shows that if the PTO hardware functioned as it was modelled, then the performance would have been two to three times higher. The study also rules out the device hydrodynamics –as set by the geometry- as the primary reason for the suboptimal performance.

Acknowledgement

Funding for this work comes from the Naval Facilities Engineering Command (NAVFAC) via the Applied Research Laboratory at UH. Early funding for these modeling efforts came from the US Department of Energy, through the Hawaii National Marine Renewable Energy Center, and from the Office of Naval Research. Key parameters relevant to the WEC devices were provided by NWEI. We would like to acknowledge Mr. Steve Kopf of NWEI for agreeing to share the research from the deployment of the Azura device, with the larger WEC community.

REFERENCES

[1] https://boltseapower.com/bolt-lifesaver-hawaii-2/

[2] B. Wu, M. Li, R. Wu, T. Chen, Y. Zhang,Y. Ye, "BBDB wave energy conversion technology and perpective in china", Ocean Enginnering 169 (2018)

[3] A. Babarit, "A database of capture width ratio of wave energy converters", *Renewable energy*, 80 (2015)

[4] P. Cross, L. Vega, K. Rajagopalan, G. Nihous, N. Li, A. Rocheleau, P. Anderson, "U.S. navy Wave Energy Test Site – Early Findings", *EWTEC*, 2017

[5] B. A. Ling, T. Lettenmaier. "WEC-SIM MODEL VALIDATION OF THE AZURA PROTOTYPE DEVICE", *Marine Energy Technology Symposium*, Washington D.C, 2016.

[6] K. Rajagopalan, P. Cross, G. Nihous, "Numerical Modeling Research at the US Navy Wave Energy Test Site, Honolulu, USA", I*SOPE* 2019.

[7] Lewis, E.V. (1989)."Volume III: Motions in Waves and Controllability". *Principles of Naval Architecture*. 1989

[8]http://cdip.ucsd.edu/?nav=historic&xitem=stn_home&stn=225

[9] WAFO group, LUND UNIVERSITY, "WAFO-a matlab Toolbox for Analysis of Random Waves and Loads", 2017.

[10] C. Ruzzo, V. Fiamma, M. Collu, G. Failla, V. Nava, F. Arena, "On intermediate-scale open-sea experiments on floating offshore structures: feasibility and application on a spar support for offshore wind turbines", *Marine Structures*, 61, (2018)

[11] K. Rajagopalan, G. Nihous, L. Vega, P. Cross, "Numerical Modeling of a Multibody WEC Using Constraint Equations", *Marine Energy Technology Symposium*, Washington D.C, US. (Poster Presentation). 2017.

[12] K. Ruehl, C. Michelen, M. Lawson, Y. Yu, S. Kanner. "Preliminary verification and validation of WEC-Sim, an open-source Wave Energy Converter design tool", *OMAE2014-24312*. (2014)

[13] L. Tao, and D. Dray" Hydrodynamic performance of solid and porous heave plates", *Ocean Engineering* 35 (2008) 1006-1014.

[14] K. Rajagopalan and G. Nihous. "Study of the force coefficients on plates using an open source numerical wave tank", *Ocean Engineering* 118 (2016) 187-203.

[15] Keulegan, G. H. and Carpenter, L. H. "Forces on Cylinders and Plates in an Oscillating Fluid", *Journal of Research of the National Bureau of Standards* 60. 1958

[16] K. Rajagopalan, P. Cross, L. Vega, "Numerical Modeling of the Lifesaver Mooring System for Deployment at WETS", *Marine Energy Technology Symposium*, 2018

[17] ANSYS, "AQWA Theory Manual", 2017

[18] R. So, S. Casey, S. Kanner, A. Simmons, T. K. A. Brekken "PTO-Sim: Development of a Power Take Off Modeling Tool for Ocean Wave Energy Conversion", *IEEE Power & Energy Society General Meeting*, 2015

[19] F. Driscoll, L. J. Fingersh, J. Weber, D. Newborn, M. Quintero, B. Gunawan, K. Ruehl, D. Bull, A. Dallman, A. LaBonte, D. Karwat, " WAVE ENERGY PRIZE TESTING AND DATA ANALYSIS OVERVIEW", *Marine Energy Technology Symposium*, Washington D.C. 2018.

[20] G. Nihous, "The Method of Imbedded Lagrangian Element to Estimate Wave Power Absorption by Some Submerged Devices", *Journal of Marine Science and Application*. 2014